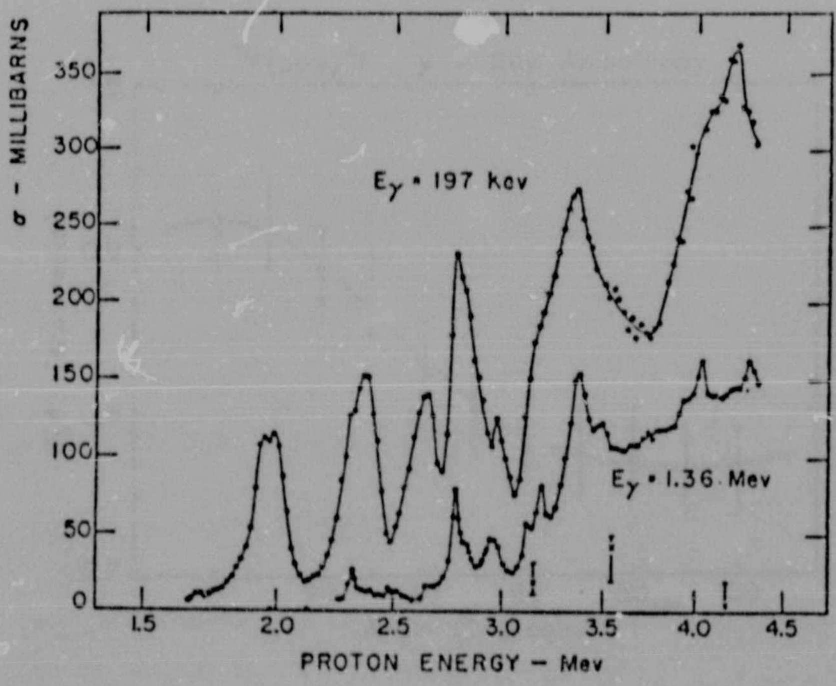

Fig. 3.3 Cross section for the 197 keV $\frac{5}{2}^+$ state of ^{19}F.

where the $A_k^\gamma(1)$ are the tabulated coefficients in the $\gamma-\gamma$ cascade case, and the unitless ξ measures the extent to which the process is adiabatic. Using calculated values for the $a_k(\xi)$ gives

$$\begin{aligned} A_2(1) &= -.225 \\ A_4(1) &= -.062 \end{aligned} \tag{3.11}$$

Alternatively, the $A_k(1)$ may be deduced from the measured angular distribution of the 197 keV γ - ray produced from the reaction ^{19}F(p,p′)^{19}F*. These data are shown in Fig. 3.4 below [Kr 78] for $E_p = 5.5$ MeV. Since these authors did not present the coefficients of the Legendre polynomials describing the distribution, their data was digitized and refitted giving

$$\begin{aligned} A_2(1)A_2(2) &= .115(15) \\ A_4(1)A_4(2) &= .0267(5) \end{aligned} \tag{3.12}$$

where the quantities in brackets are the errors. The resulting $A_k(1)$ are

$$\begin{aligned} A_2(1) &= -.215(15) \\ A_4(1) &= -.0433(5) \end{aligned} \tag{3.13}$$

The two methods agree well for $k = 2$ and reasonably well for $k = 4$. The anisotropy is about 14%. Note that none of the A_k are sufficiently small to be neglected.

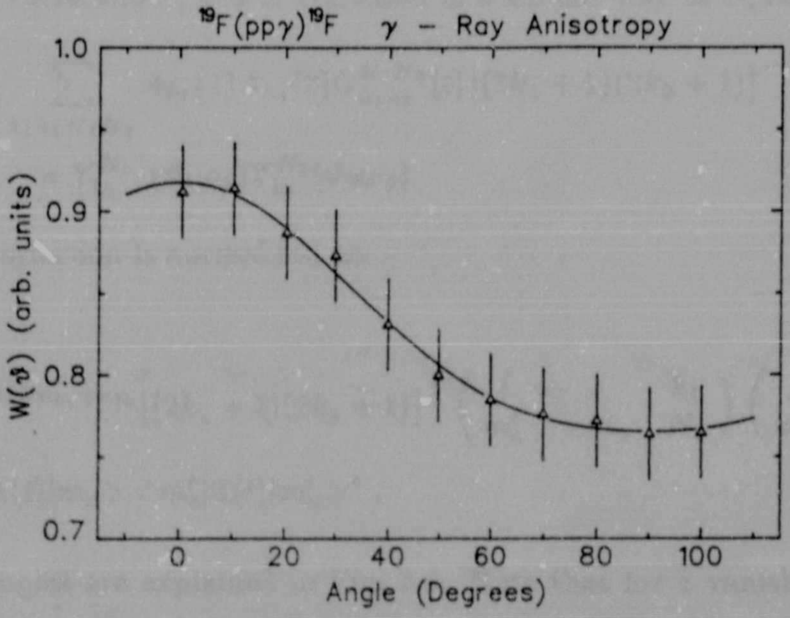

Fig. 3.4 Angular distribution for the 197 keV γ - ray in the reaction ^{19}F(p,p′)^{19}F* at $E_p = 5.5$ MeV.

Adding the perturbation

Suppose the intermediate state I exists for a time t in the presence of an external field, described by the Hamiltonian K. During this time the intermediate level substates $|m_a\!>$ transform into the states $|m_b\!>$ under the influence of the time evolution operator $\Lambda(t)$ (Fig. 3.5), which for static interactions is written

$$\Lambda(t) = e^{-\frac{iKt}{\hbar}}. \tag{3.14}$$

The angular correlation expression of equation (3.5) becomes

$$\begin{aligned} W(\mathbf{k}_1,\mathbf{k}_2) &= S_1S_2 \sum_{m_f m_a m'_a m_i} <m_f|H_2\Lambda(t)|m_a><m_a|H_1|m_i> \\ &\qquad \times <m'_a|H_1|m_i>^*<m_f|H_2\Lambda(t)|m'_a>^* \\ &= S_1S_2 \sum_{\substack{m_f m_i \\ m_a m_b m'_a m'_b}} <m_f|H_2|m_b><m_b|\Lambda(t)|m_a><m_a|H_1|m_i> \\ &\qquad \times <m_f|H_2|m'_b>^*<m'_b|\Lambda(t)|m'_a>^*<m'_a|H_1|m_i>^* . \end{aligned} \tag{3.15}$$

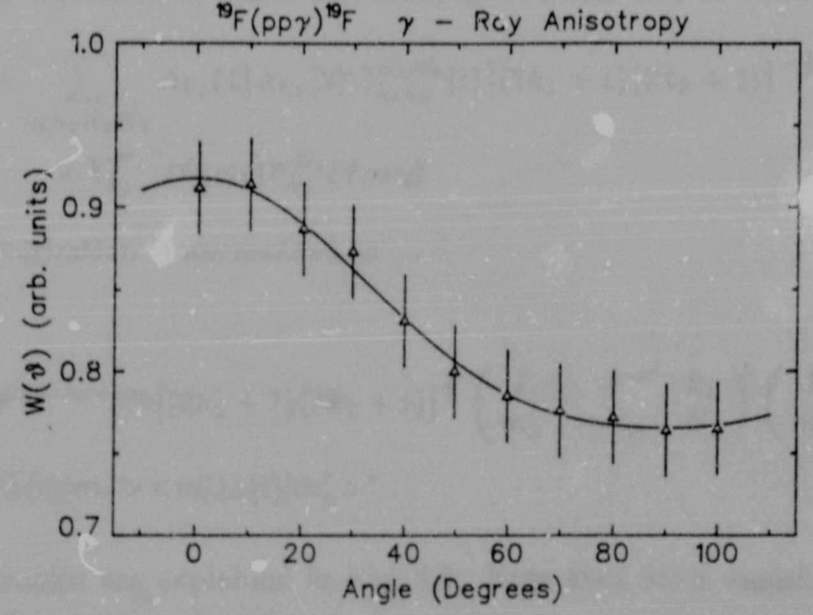

Fig. 3.4 Angular distribution for the 197 keV γ - ray in the reaction $^{19}\mathrm{F(p,p')}^{19}\mathrm{F}^*$ at $E_p = 5.5$ MeV.

Adding the perturbation

Suppose the intermediate state I exists for a time t in the presence of an external field, described by the Hamiltonian K. During this time the intermediate level substates $|m_a>$ transform into the states $|m_b>$ under the influence of the time evolution operator $\Lambda(t)$ (Fig. 3.5), which for static interactions is written

$$\Lambda(t) = e^{-\frac{iKt}{\hbar}}. \tag{3.14}$$

The angular correlation expression of equation (3.5) becomes

$$\begin{aligned} W(\mathbf{k}_1,\mathbf{k}_2) &= S_1S_2 \sum_{m_f m_a m'_a m_i} <m_f|H_2\Lambda(t)|m_a><m_a|H_1|m_i> \\ &\qquad \times <m'_a|H_1|m_i>^*<m_f|H_2\Lambda(t)|m'_a>^* \\ &= S_1S_2 \sum_{\substack{m_f m_i \\ m_a m_b m'_a m'_b}} <m_f|H_2|m_b><m_b|\Lambda(t)|m_a><m_a|H_1|m_i> \\ &\qquad \times <m_f|H_2|m'_b>^*<m'_b|\Lambda(t)|m'_a>^*<m'_a|H_1|m_i>^* . \end{aligned} \tag{3.15}$$

For directional correlations, this is evaluated in a similar way to equation (3.7) to give

$$W(\mathbf{k}_1, \mathbf{k}_2; t) = \sum_{k_1 k_2 N_1 N_2} A_{k_1}(1) A_{k_2}(2) G^{N_1 N_2}_{k_1 k_2}(t) \left[(2k_1+1)(2k_2+1)\right]^{-\frac{1}{2}} \times Y^{N_1 *}_{k_1}(\vartheta_1 \varphi_1) Y^{N_2}_{k_2}(\vartheta_2 \varphi_2) \tag{3.16}$$

where the perturbation is normalized as

$$G^{N_1 N_2}_{k_1 k_2}(t) = \sum_{m_a m_b} (-1)^{2I+m_a+m_b} \left[(2k_1+1)(2k_2+1)\right]^{\frac{1}{2}} \begin{pmatrix} I & I & k_1 \\ m'_a & -m_a & N_1 \end{pmatrix} \begin{pmatrix} I & I & k_2 \\ m'_b & -m_b & N_2 \end{pmatrix} \times \langle m_b | \Lambda(t) | m_a \rangle \langle m'_b | \Lambda(t) | m'_a \rangle^* . \tag{3.17}$$

The relevant angles are explained in Fig. 3.6. Note that for a vanishing perturbation ($t = 0$) the orthogonality of the $3 - j$ symbols gives

$$G^{N_1 N_2}_{k_1 k_2} \equiv \delta_{k_1 k_2} \delta_{N_1 N_2}, \tag{3.18}$$

and the addition theorem of the spherical harmonics restores equation (3.16) to its unperturbed form (3.7).

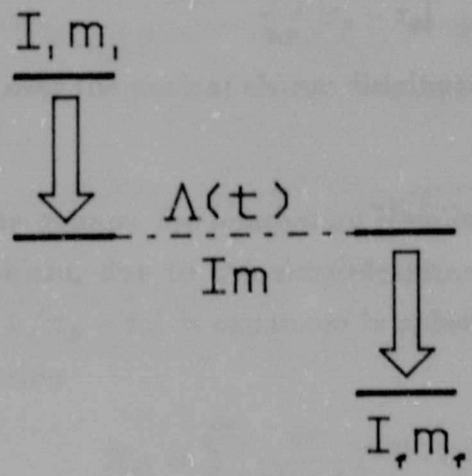

Fig. 3.5 Double decay cascade where the intermediate level is perturbed by an extra-nuclear field.

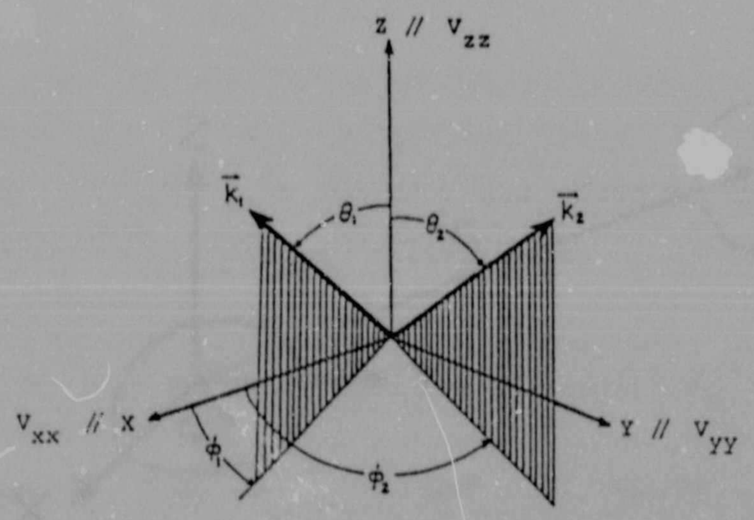

Fig. 3.6 Angles relevant to the directional correlation (3.16).

The Electric Field Gradient

This section evaluates the matrix elements of the perturbation Hamiltonian in the case of the extra-nuclear field being the electric field gradient (efg) [Ma 62, Ka 73]. For electric static interactions the Hamiltonian is

$$H_{\mathrm{el}} = \sum_{c,p} \frac{e_p e_c}{|\mathbf{r}_p - \mathbf{r}_c|} \tag{3.19}$$

where the index p runs over the nuclear charge distribution and c over the crystal charge distribution (Fig. 3.7).

It is usually wise to express the interaction Hamiltonian in a way that reflects the symmetries of the problem, due to the simplifications that result. To this end, the point charge potential $1/|\mathbf{r}_p - \mathbf{r}_c|$ is expanded in spherical harmonics. This allows the factoring of the interaction

$$H_{\mathrm{el}} = \sum_{k=0}^{\infty} \frac{4\pi}{2k+1} T^{(k)} \cdot V^{(k)} \tag{3.20}$$

with

$$\begin{aligned} T_q^{(k)} &= \sum_p e_p r_p^k Y_k^q(\vartheta_p, \varphi_p), \\ V_q^{(k)} &= \sum_c e_c \frac{1}{r_c^{k+1}} Y_k^q(\vartheta_c, \varphi_c). \end{aligned} \tag{3.21}$$

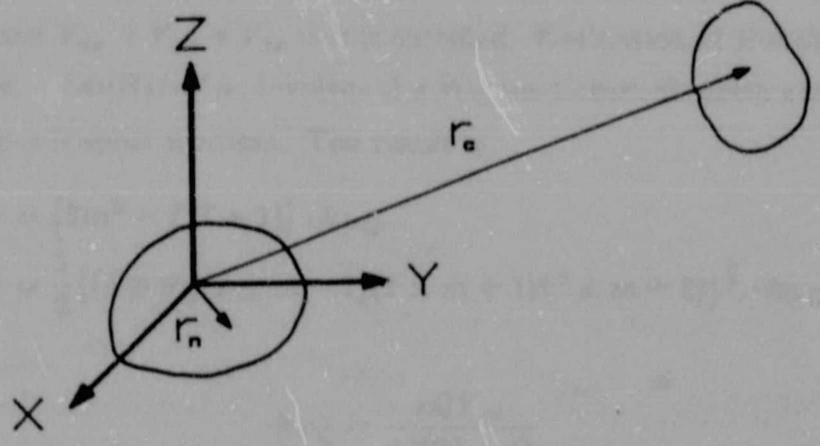

Fig. 3.7 Position vectors for the electric interaction.

The lack of q indices in equation (3.20) implies that they have been summed out in the spherical tensor scalar product. This formalism conveniently expresses the interaction as a multipole series consisting of products of nuclear and crystal factors. The first term is the ordinary coulomb potential which does not lead to transitions among the substates. The dipole and octopole terms have zero expectation values (π conservation) and higher multipoles are neglected. The electric interaction Hamiltonian thus reduces to only the quadrupole interaction with the electric field gradient

$$\begin{aligned} K = H_{efg} &= \frac{4\pi}{5} T^{(2)} \cdot V^{(2)} \\ &= \frac{4\pi}{5} \sum_q (-1)^q T_q^{(2)} V_{-q}^{(2)} \end{aligned} \tag{3.22}$$

If the cartesian components of the efg are evaluated in the principal axis system where the efg tensor is diagonal with $|V_{zz}| \geq |V_{yy}| \geq |V_{xx}|$ and the efg asymmetry parameter is defined

$$\eta = (V_{xx} - V_{yy}) / V_{zz} \tag{3.23}$$

then the spherical tensor $V_q^{(2)}$ is

$$\begin{aligned} V_0^{(2)} &= \frac{1}{4}\sqrt{\frac{5}{\pi}} V_{zz}, \\ V_{\pm1}^{(2)} &= 0, \\ V_{\pm2}^{(2)} &= \frac{1}{4}\sqrt{\frac{5}{6\pi}} \eta V_{zz}. \end{aligned} \tag{3.24}$$

Note that V_{zz}, η and $(\theta, \phi)_{efg}$, the efg orientation, completely specify the efg since Poisson's equation $V_{xx} + V_{yy} + V_{zz} = 0$ is satisfied. Evaluation of the efg spin substate matrix elements, $<Im|K|Im'>$, involves the Wigner-Eckart theorem and the definition of the nuclear quadrupole moment. The result is

$$\begin{aligned} <m|K|m> &= \left[3m^2 - I(I+1)\right] \cdot \hbar\omega_Q \\ <m \pm 2|K|m> &= \frac{1}{2}\left[(I \mp m)(I \mp m - 1)(I \pm m + 1)(I \pm m + 2)\right]^{\frac{1}{2}} \cdot \hbar\omega_Q \cdot \eta \end{aligned} \tag{3.25}$$

where

$$\hbar\omega_Q = \frac{eQV_{zz}}{4I(2I-1)} \tag{3.26}$$

Single Crystal Formalism

The expression for the perturbed angular directional correlation given above in equations (3.16) and (3.17) applies to all static interactions involving classical fields. When the interaction and system symmetries are specified, it can be simplified. Paper 2 of the Results and Conclusions shows that in the general case of $\gamma - \gamma$ correlations involving static electric quadrupole interactions, the perturbation function can always be expressed as a sum of cosine terms, without having to make any assumption about the axial symmetry of the perturbing field or employing the averaging procedure used in the case of polycrystalline hosts.

$$G_{k_1k_2}^{N_1N_2}(t) = \sum_{nn'} S_{k_1k_2}^{N_1N_2}(n,n') \cos(\omega_{n,n'}t) \tag{3.27}$$

where the S coefficients are defined

$$\begin{aligned} &S_{k_1k_2}^{N_1N_2}(n,n') = \\ &\quad \sum_{m_a m_b} (-1)^{2I+m_a+m_b} \left[(2k_1+1)(2k_2+1)\right]^{\frac{1}{2}} \begin{pmatrix} I & I & k_1 \\ m_a' & -m_a & N_1 \end{pmatrix} \begin{pmatrix} I & I & k_2 \\ m_b' & -m_b & N_2 \end{pmatrix} \\ &\quad \times <n|m_b>^* <n|m_a> <n'|m_b'> <n'|m_a'>^* . \end{aligned} \tag{3.28}$$

The $<n|m>$ are unitary matrix elements diagonalizing K and the $\omega_{n,n'}$ frequencies correspond to the level splitting $E_n - E_{n'}$ where E_n are the eigenvalues of K. Though many have used this fact, the formal justification for it in this most general case has not been presented before.

The correlation depends on the angles ϑ and φ (viz., the polar and azimuthal angle of the efg with respect to the detector plane) through the dependency of the spherical harmonics. Since there are many equivalent crystallographic directions for a given choice of crystal axes for the efg components, the correlation must be averaged over all of these [We 85], i.e.

$$\left[(2k_1+1)(2k_2+1)\right]^{-\frac{1}{2}}\left\{\frac{1}{L}\sum_{i,j}^{L} Y_{k_1}^{N_1\,*}(\vartheta_i\varphi_i)Y_{k_2}^{N_2}(\vartheta_j\varphi_j)\right\}. \tag{3.29}$$

It is thus convenient to define $S^{\text{eff}}_{k_1k_2}$ which contains the geometry-dependent averaged spherical harmonic component with the N indices summed out. The sum over n, n' can be broken up into groups with the same frequency

$$S^{N_1N_2}_{k_1k_2p} = {\sum_{nn'}}' S^{N_1N_2}_{k_1k_2}(n,n') \tag{3.30}$$

where the prime on the summation indicates that it is restricted to values of n and n' leading to the same frequency. The integer p labels the distinct frequencies defined by

$$\begin{aligned}(E_n - E_{n'})/\hbar &= \omega_{nn'}\\ &= g_p\omega_0.\end{aligned} \tag{3.31}$$

ω_0 is the smallest non-vanishing frequency related to the quadrupole frequency ω_Q by

$$\omega_0 = \begin{cases} 3\omega_Q, & \text{for integer I}\\ 6\omega_Q, & \text{for half-integer I.}\end{cases} \tag{3.32}$$

Hence

$$\begin{aligned}W(\mathbf{k}_1,\mathbf{k}_2;t) &= W(\vartheta,\varphi,\theta;t)\\ &= 1+\sum_{\substack{k_1k_2\\p}} A_{k_1k_2}S^{\text{eff}}_{k_1k_2p}(\vartheta,\varphi,\theta)\cos(g_p\omega_0t)\\ &= 1+\sum_{k_1k_2} A_{k_1k_2}G^{\text{eff}}_{k_1k_2}(\vartheta,\varphi,\theta;t).\end{aligned} \tag{3.33}$$

The $S^{\text{eff}}_{k_1k_2p}$ may be regarded as Fourier coefficients in a decomposition of the perturbation, although this is not a proper Fourier transform as the frequencies are not necessarily integral multiples of the fundamental frequency.

Explicitly for $I = \frac{5}{2}^+$

For the case $I = \frac{5}{2}$ of ^{19}F*, the eigenvalues are degenerate, $E_n = E_{-n}$. The distinct frequencies resulting, ω_p, are labelled by $p = \frac{1}{2}\left|n^2 - n'^2\right|$. The Hamiltonian K may be diagonalized analytically [Ka 73] yielding the following expressions for the eigenvalues and unitary matrix elements :

$$E_n = 2\left[28\left(1+\frac{\eta^2}{3}\right)\right]^{\frac{1}{2}} \hbar\omega_Q \cdot \begin{cases} \cos\Phi\,/3\,, & n = \pm\frac{5}{2} \\ \cos(\Phi+\pi)\,/3\,, & n = \pm\frac{3}{2} \\ \cos(\Phi-\pi)\,/3\,, & n = \pm\frac{1}{2} \end{cases} \tag{3.34}$$

with

$$\Phi = \arccos \frac{80\left(1-\eta^2\right)}{\left[28\left(1+\eta^2/3\right)\right]^{3/2}} \tag{3.35}$$

$$\begin{aligned} <n|\tfrac{1}{2}> &= \left[1 + 10\eta^2 \Big/ \left(10 - \frac{E_n}{\hbar\omega_Q}\right)^2 + 18\eta^2 \Big/ \left(-2 - \frac{E_n}{\hbar\omega_Q}\right)^2\right]^{-\frac{1}{2}} \\ <n|-\tfrac{3}{2}> &= -\sqrt{18}\eta <n|\tfrac{1}{2}> \left(-2 - \frac{E_n}{\hbar\omega_Q}\right) \\ <n|\tfrac{5}{2}> &= -\sqrt{10}\eta <n|\tfrac{1}{2}> \left(10 - \frac{E_n}{\hbar\omega_Q}\right) \end{aligned} \tag{3.36}$$

where $n = \frac{5}{2}, \frac{1}{2}, -\frac{3}{2}$, $<n|m> = <-n|-m>$ and all other matrix elements vanish. Fig. 3.8 summarizes the excitation of the ^{19}F, the splitting of the $\frac{5}{2}$ levels by the electric quadrupole interaction as a function of efg asymmetry and the transitions occurring between the substates which lead to the perturbation of the correlation. Note that the *magnitude and asymmetry* of the efg give the observed PAC *frequencies*. The *intensities* with which these frequencies are present will given by the geometric factors $S^{\text{eff}}_{k_1k_2p}$ which allow the efg *orientation* to be deduced.

Simulations

For technical reasons the TDPAD data to be simulated are normally presented as

$$R_{\text{exp}}(t) = 2\frac{N(0^\circ,t) - N(90^\circ,t)}{N(0^\circ,t) + 2N(90^\circ,t)} \tag{3.37}$$

where $N(0^\circ,t)$ and $N(90^\circ,t)$ are the observed normalized count rate to be approximated by

$$N(\theta,t) = N \cdot W(\vartheta,\varphi,\theta;t)\cdot\exp(-t/\tau) + B. \tag{3.38}$$

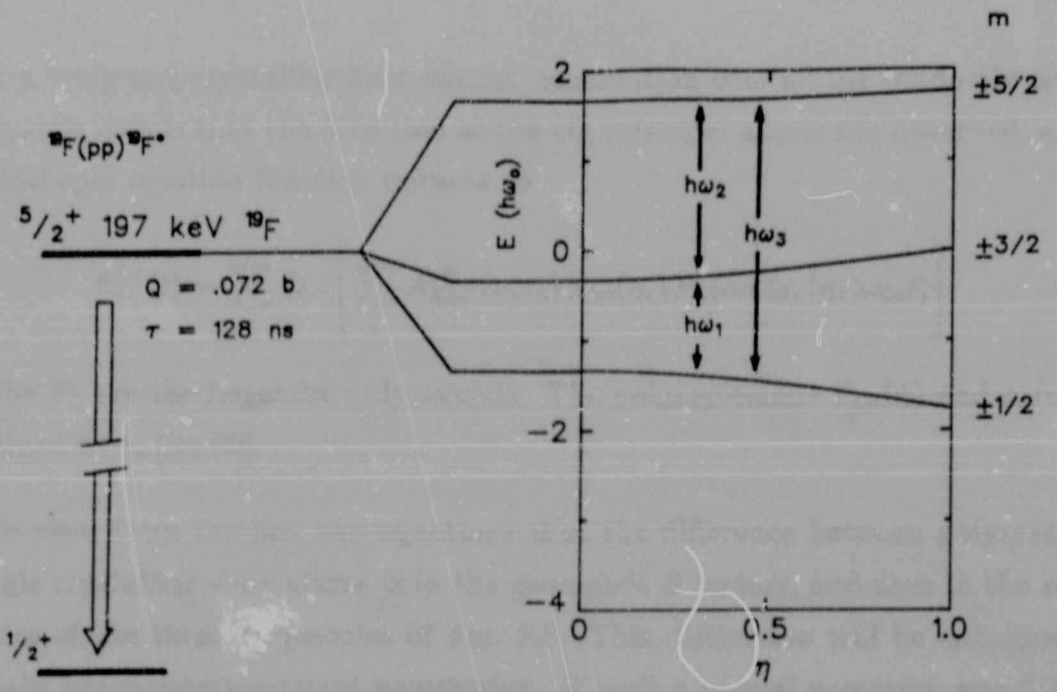

Fig. 3.8 Quadrupole splitting of the ^{19}F $\frac{5}{2}$ level as a function of efg asymmetry.

Assuming the background B and normalization N have been removed, we have for single crystals to a good approximation [We 85]

$$R^{\mathrm{sc}}_{\mathrm{th}}(t) = \frac{2}{3} \cdot \sum_i f_i \cdot \left[\sum_{k_1,k_2} A^{\mathrm{eff}}_{k_1 k_2} f(\sigma, \delta_i) \hat{G}^{\mathrm{eff}}_{k_1 k_2}(\vartheta_i, \varphi_i, \eta_i, \omega_{0i}; t) \right] \tag{3.39}$$

where

$$\hat{G}^{\mathrm{eff}}_{k_1 k_2}(\vartheta, \varphi; t) = G^{\mathrm{eff}}_{k_1 k_2}(\vartheta, \varphi, 0^\circ; t) - G^{\mathrm{eff}}_{k_1 k_2}(\vartheta, \varphi, 90^\circ; t). \tag{3.40}$$

The $A^{\mathrm{eff}}_{k_1 k_2}$ are the usual anisotropy coefficients corrected for solid angle effects [Si 65b]. Allowance has been made for probe ions occupying a variety of unique sites; f_i being the fraction of implants at the site i. The amplitude attenuation factor $f(\sigma, \delta_i)$ has been included to take account of the finite time resolution σ of the detection system and a possible spread δ_i for the efg at that site [Be 69]. The data is fitted with the theoretical function (3.39) which extracts for each site its population fraction f_i, frequency ω_{0i}, asymmetry parameter η_i, efg spread δ_i and efg crystallographic orientation (ϑ_i, φ_i) The difference between this presentation and that of [We 85] is that it was not considered possible to neglect the $A_4(1)$ anisotropy coefficient for the ^{19}F case and so all the geometric factors $S^{\mathrm{eff}}_{k_1 k_2 p}$ were calculated. (see paper 1 of the Results and Conclusions and Appendix 1).

For a truly polycrystalline host matrix, summation over all the randomly oriented microcrystals means that the direction of the efg principal axis is not observed, and the theoretical spin rotation function reduces to

$$R_{\mathrm{th}}^{\mathrm{pc}}(t) = \sum_i f_i \cdot \left[\sum_k A_{kk}^{\mathrm{eff}} f(\sigma, \delta_i) S_{kp}(\eta_i) P_k(\cos(g_p(\eta_i)\omega_{0i}t) \right] \tag{3.41}$$

where the P_k are the Legendre polynomials. The polycrystalline $S_{kp}(\eta)$ and $g_p(\eta)$ may be obtained from [Be 69].

It is clear from the last two equations that the difference between polycrystalline and single crystalline simulations is in the geometric S factors, and thus in the relative intensities of the three frequencies of Fig. 3.8. This distinction will be enhanced only for certain beam-detector-target geometries. If such a special geometry was found, it would increase the measurement sensitivity of the TDPAD technique to slight polycrystalline effects in single crystals. This technique was used in paper 3 of the results and conclusions. Other theoretical simulations are to be found in Paper 1 of the same chapter.

CHAPTER 4.
EXPERIMENTAL (TDPAD)

Contents

Introduction

A summary of the experimental layout of an in-beam TDPAD experiment is presented schematically in Fig. 4.1 below.

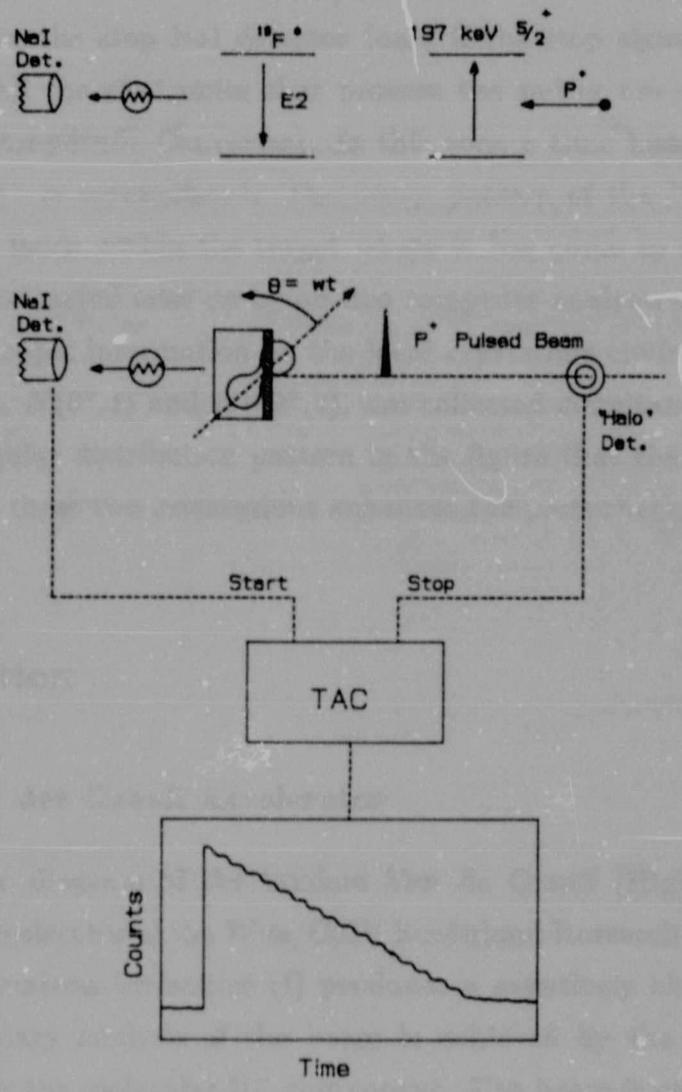

Fig. 4.1 Schematic representation of TDPAD measurements using ^{19}F recoil implantation.

The essential components are a pulsed MeV proton source, detection equipment and associated electronics, and a target consisting of the material to be studied, with an evaporated probe layer on its upstream surface. The figure displays the simultaneous excitation of the 197 keV $\frac{5}{2}^+$ state of fluorine, ^{19}F*, and the recoil implantation of the ^{19}F probe into the host lattice. The proton beam is pulsed so that the time of detection of the de-excitation γ-ray can be measured from the correlated arrival of a sharp intense beam pulse. One event thus corresponds to a time measurement between a signal from the start "halo" detector (which fires when a beam pulse passes through) and a signal from the stop NaI detector (only if the stop signal corresponds to a 197 keV γ - ray). All the electronics that process the pulses are summarized in the box TAC (Time to Amplitude Converter). In this way, a time histogram representing the decay of the ^{19}F* is accumulated. The decay pattern of the ^{19}F is perturbed by the local crystalline fields within the target where it has come to rest. The perturbation pattern can be extracted later on by off-line computer analysis of the decay spectra. In this way, microscopic information on the local crystalline environment is obtained. In fact two spectra, $N(0°,t)$ and $N(90°,t)$, are collected simultaneously. It is clear from the rotating angular distribution pattern in the figure that the difference between the spectra taken at these two orientations enhances the perturbation superimposed on the decay curves.

Data generation

Tandem Van der Graaff Accelerator

A schematic diagram of the tandem Van de Graaff (High Voltage Engineering, model EN 30) accelerator of the Wits/CSIR Schönland Research Centre is shown in Fig. 4.2. A Duoplasmatron ion source (I) produces a negatively charged beam of protons at 80 keV. Primary analysis of the beam is achieved by the inflection magnet (M) which was set for the molecular H_2^- component. The beam is chopped and bunched by components (C) and (B) and fed into the Tandem Van de Graaff accelerator (A). The terminal voltage is +2 MV and the stripping to a p^+ beam is by ionization interactions in a $10\,\mu g/cm^2$ carbon foil at the centre terminal. After acceleration, the 4 MeV beam passes through the analysing magnet (M), with the slits opened wide since some energy resolution, which is not important, is sacrificed for beam intensity. The switching magnet (M) directs the pulsed beam into the 15° West target beamline where the TDPAD detectors are mounted. The start detector (S) is 2m upstream of the target (T). The detectors are mounted on an extremely stable platform which allows highly reproducible interchanging of the 0° and 90° detectors simply by a 90° rotation of the detector carriages. Each TDPAD measurement of ≈ 30 hours was broken down into successive measurements of about 4 hours each with the detector positions interchanged, to enable the cancellation of detector efficiencies from the spin rotation spectra $R(t)$ [Ar 80].

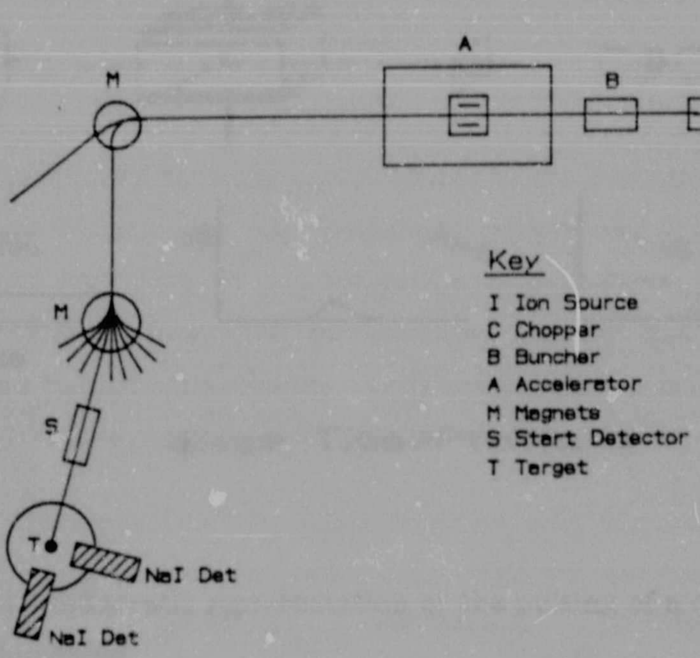

Fig. 4.2 Schematic representation of TDPAD set-up on the Wits/CSIR Schönland Research Centre tandem Van de Graaff accelerator.

Beam Pulser

The beam pulsing system consists of a chopper and buncher, both situated at the low energy side of the machine. Continuous beam is chopped (electrostatically) into short sections (6 - 20 ns) separated by longer intervals of no beam (.25 - 2 μs). The chopped beam is fed into a phase locked buncher which operates by decelerating the leading edge of the beam "sausage" and accelerating its trailing end. These accelerations only occur while the beam is in the buncher. The actual bunching takes place mostly during the low-energy drift of the "sausage" where the correctly adjusted differential velocities of its front and back part cause it to become gradually compressed. The "sausage" will only be a sharp intense pulse by the time it arrives at the target station. Fig. 4.3 depicts this process schematically.

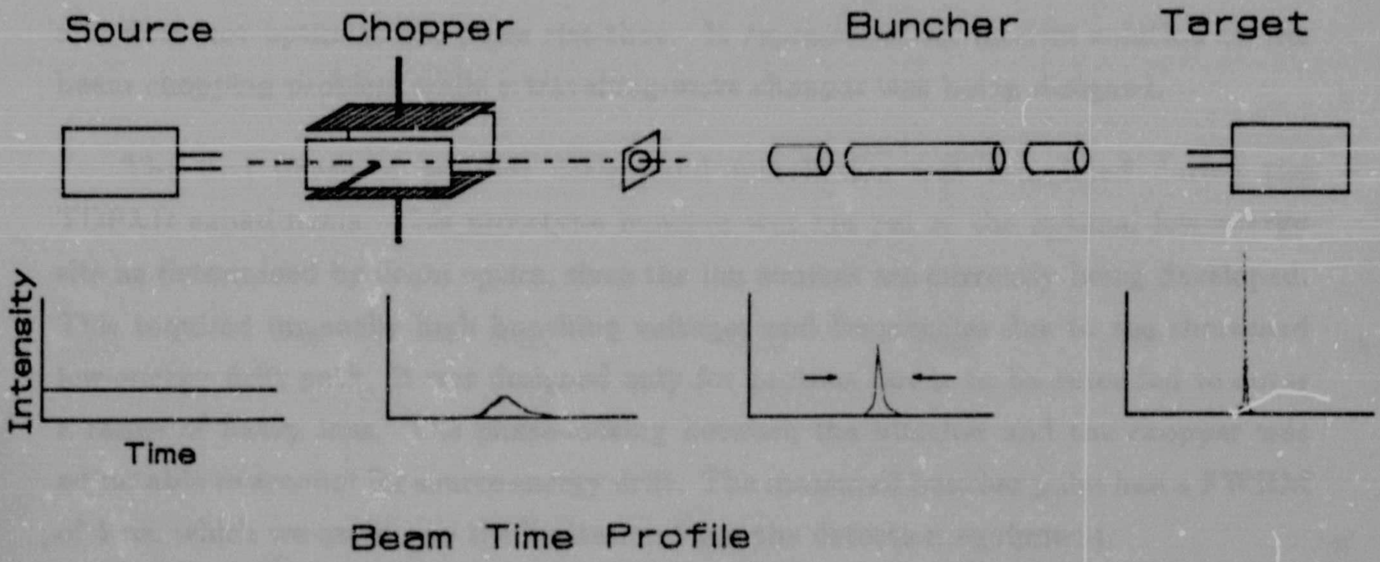

Fig. 4.3 Schematic representation of the pulsing of a continuous beam by chopping and bunching.

The current chopper at the SRCNS has a set of vertical and horizontal electrostatic deflection plates. In principle, a pattern similar to a Lissajous figure is traced out by the beam, which passes through the chopping aperture only for certain pre-defined voltages, frequencies and relative phases of the signals applied to the deflection plates. Adjustment of these parameters allows the beam pulse repetition rate and the beam pulse length to be pre-set. The potential on each plate may be set to a maximum of 800 V measured at the feed-throughs. This maximum is determined more by the deflected beam striking the plates than by technical limitations. The vertical sweep is a sine wave with a fixed frequency of 8 MHz. The horizontal sweep approximates a square wave, the frequency of which may be set to various integer sub-multiples of the vertical sweep frequency, in order to select the chopped beam repetition rate. The pulse length was varied by adjusting the sweep voltages. The centring of the beam "Lissajous" figure on the chopping aperture was achieved by biasing the floating potentials fed to the electrostatic deflection plates. The phase between the vertical and horizontal plates was variable from $0 - 2\pi$ in order to compensate for beam transport time between the plates and to symmetrize the "Lissajous" figure. Repetition periods from .25 - 2 μs are possible with beam pulse lengths of 6 - 20 ns. In practice the system was reliable and easy to use, though it had the disadvantage of delivering off-axis beam to the machine and does not optimize the pulse rise-time. It represented an interim solution to the beam chopping problem while a travelling-wave chopper was being designed.

The first phase of buncher design and installation was completed during the TDPAD experiments. This prototype buncher was not yet at the optimal low energy site as determined by beam optics, since the ion sources are currently being developed. This required unusually high bunching voltages and frequencies due to the shortened low-energy drift path. It was designed only for protons but is to be extended to cover a range of heavy ions. The phase-locking between the buncher and the chopper was adjustable to account for source energy drift. The measured buncher pulse had a FWHM of 4 ns, which we ascribe to the limitation from the detection equipment.

All the controls of the beam chopping and bunching were located in the control room. Observation of the pulsed beam directly via the halo detector output enabled the system to be set up within minutes and continuously monitored throughout the experiment, although its stability over a 30 hour period was usually within the time resolution.

Halo Start Detector

Many systems for detecting the arrival of a beam pulse were installed and tested in order of increasing complexity. The first system consisted of a charge sensitive detector connected to a thin foil. At the beam currents applicable to a TDPAD experiment, the signal from the delta electrons ejected by the beam passage did not appear sufficiently high above the noise level. A capacitive pick-up was eventually rejected for the same reason. Currently, a scintillating disc with a hole provided for the transmission of the beam is installed. The unfocussed "halo" of the beam clips the scintillator material as it passes through. A 14-stage photo-multiplier tube, not directly coupled to the scintillator, but viewing it from a reverse geometry, provided the beam pulse arrival signal. The upstream side of the scintillator had a 1.5-2 $\mu g\,cm^{-2}$ coating of gold

Author Connell S H
Name of thesis Internal Fields in Diamond and Related Materials 1988

PUBLISHER:

University of the Witwatersrand, Johannesburg
©2013

LEGAL NOTICES:

Copyright Notice: All materials on the University of the Witwatersrand, Johannesburg Library website are protected by South African copyright law and may not be distributed, transmitted, displayed, or otherwise published in any format, without the prior written permission of the copyright owner.

Disclaimer and Terms of Use: Provided that you maintain all copyright and other notices contained therein, you may download material (one machine readable copy and one print copy per page) for your personal and/or educational non-commercial use only.

The University of the Witwatersrand, Johannesburg, is not responsible for any errors or omissions and excludes any and all liability for any errors in or omissions from the information on the Library website.